Nanoscale

PAPER

View Article Online
View Journal | View Issue

Cite this: *Nanoscale*, 2014, **6**, 12682

Two-dimensional layered semiconductor/graphene heterostructures for solar photovoltaic applications

Mariyappan Shanmugam, Robin Jacobs-Gedrim, Eui Sang Song and Bin Yu*

Received 16th June 2014,
Accepted 19th August 2014

DOI: 10.1039/c4nr03334e

www.rsc.org/nanoscale

Schottky barriers formed by graphene (monolayer, bilayer, and multilayer) on 2D layered semiconductor tungsten disulfide (WS_2) nanosheets are explored for solar energy harvesting. The characteristics of the graphene–WS_2 Schottky junction vary significantly with the number of graphene layers on WS_2, resulting in differences in solar cell performance. Compared with monolayer or stacked bilayer graphene, multilayer graphene helps in achieving improved solar cell performance due to superior electrical conductivity. The all-layered-material Schottky barrier solar cell employing WS_2 as a photoactive semiconductor exhibits efficient photon absorption in the visible spectral range, yielding 3.3% photoelectric conversion efficiency with multilayer graphene as the Schottky contact. Carrier transport at the graphene/WS_2 interface and the interfacial recombination process in the Schottky barrier solar cells are examined.

Introduction

Recently, 2D layered semiconductors have been rapidly emerging as a new class of functional materials for various applications such as nanoelectronics,[1–6] solar cells,[7–9] photodetectors[10–12] and energy storage.[13–16] Compared with traditional semiconductors such as Si,[17] GaAs,[18] CdTe,[19] and $CuInSe_2$,[20] mechanical flexibility,[21] tunable optical bandgap,[22] and high carrier mobility[23] are among the few intriguing properties that warrant considering 2D layered semiconductors as potential candidates in solar energy harvesting. Tungsten disulfide (WS_2), one of the members in the 2D layered semiconductor family, has been recently explored for various nanodevice applications.[24–26] Its tunable optoelectronic properties offer unique opportunities in developing efficient solar photovoltaic technology. The major advantages of 2D layered semiconductors, such as improved photo-response and layer-dependent optical/electrical properties, have been reported for various optoelectronics applications.[27,28]

It is evident that by changing the number of layers of 2D semiconductors in a stack, photons with a wide spectral range can be harvested to generate electrons. In 2D semiconductors, weak van der Waals forces bring individual atomic planes together, while strong covalent bonds exist within each crystal plane.[29] This allows for easy exfoliation of 2D crystals to make devices. However, the exfoliation process[30,31] yields sheets with only a small area. Recently, the chemical vapour deposition (CVD) method has been demonstrated for large-area growth.[32–34] On the other hand, the superior properties of graphene such as high carrier mobility[35] and negligible photo-absorption[36] in the visible spectral range are considered to be key merits in serving as a transparent conductor for solar cells.[37] The characteristics of graphene vary to a great extent among monolayer, bilayer, and multilayer graphenes.[38] Graphene stacked with 2D semiconductors in heterostructures has been explored for applications in electronics to demonstrate the possibility of incorporating the advantages of both materials.[39–42]

Schottky barrier solar cells are relatively simple in the structure and fabrication process, as compared with p–n, p–i–n, and tandem solar cells, having only a metal–semiconductor junction to establish a built-in electric field in the depleted semiconductor region. Recently, extraordinary photon absorption has been reported in 2D semiconductors in only a few atomic layers.[43] In Schottky barrier solar cells, a strong electric field at the metal/semiconductor junction, a defect-free interface (to avoid Fermi level pinning), efficient photo-absorption and carrier transport are key factors to achieve high performance. In general, 2D layered semiconductors exhibit self-terminated atomic planes with no unsaturated dangling bonds at the surface, which helps in facilitating the formation of a high-quality interface and to achieve efficient carrier transport with negligible interfacial traps. In this research paper, we study the characteristics of the graphene/WS_2 Schottky barrier in the solar cell structure. The impacts of graphene layered configurations on the photovoltaic performance of the Schottky barrier solar cell are examined.

College of Nanoscale Science and Engineering, State University of New York, Albany, NY-12203, USA. E-mail: byu@albany.edu; Fax: +(518) 956-7492; Tel: +(518) 956-7492

Experimental

CVD growth of WS_2 nanosheet

Tungsten (W) film with a thickness of ~30 nm was deposited onto SiO_2-coated Si substrates by electron-beam evaporation. The W-coated substrates were placed downstream in the CVD quartz tube chamber. Sulfur powder (99.99% purity) was placed upstream in the chamber. Sulfur was evaporated at 115 °C with 200 sccm flow of argon as the carrier gas. The chamber pressure was maintained at 1 Torr. Solid–vapour reaction between the tungsten surface and sulfur vapour resulted in WS_2 nanosheets on Si/SiO_2 substrates. A 1000 °C post-annealing treatment was performed for one hour to improve the crystallinity of WS_2 samples. Fig. 1(a) shows the schematic diagram of the CVD furnace set-up used for WS_2 growth. Note the two temperature zones used for sulfur evaporation and WS_2 growth. Fig. 1(b) is the photograph of a typical sample showing large-area growth of WS_2 on SiO_2. Fig. 1(c) illustrates the planar hexagonal lattice structure of WS_2 composed of W and S atoms in the 2D crystal plane.

Polymethyl methacrylate (PMMA) was coated on WS_2, as the supporting material to facilitate the transfer process. The sample was annealed at 90 °C for 5 minutes. Potassium hydroxide (KOH) was used to etch the SiO_2 layer, releasing WS_2 nanosheets from Si substrates and making it free-floating in KOH. The free-floating WS_2 nanosheet was manually transferred from KOH to aluminum (Al) coated glass substrate for solar cell fabrication. This method is feasible for large-area grown samples of 2D semiconductors. The etching rate of SiO_2 is determined by the KOH concentration. A fast etching rate may affect the material quality of 2D semiconductors. Therefore, it is important to use a seamless etching process to minimize process-induced effects on WS_2 nanosheets.

CVD growth of graphene

Growth of monolayer and multilayer graphene was performed by the CVD method using Cu and Ni as the substrates, respectively. Methane and hydrogen gases were used to take advantage of the solubility of carbon in Cu and Ni substrates, resulting in monolayer and multilayers of graphene, respectively. The growth temperature was fixed at 1000 °C for both monolayer and multilayer graphene growth. The PMMA layer was coated on the graphene-grown Cu and Ni substrates by the spin coating method at 2000 rpm for 1 minute, followed by a baking at 90 °C for 5 minutes. The Cu and Ni substrates were etched by a $FeCl_3$ solution. The separated graphene films were then transferred to deionized water to remove excessive $FeCl_3$ on the surface. Subsequently, the PMMA-supported monolayer and multilayer graphene layers were transferred onto WS_2 nanosheets for solar cell fabrication. After transferring graphene, the PMMA was dissolved by acetone.

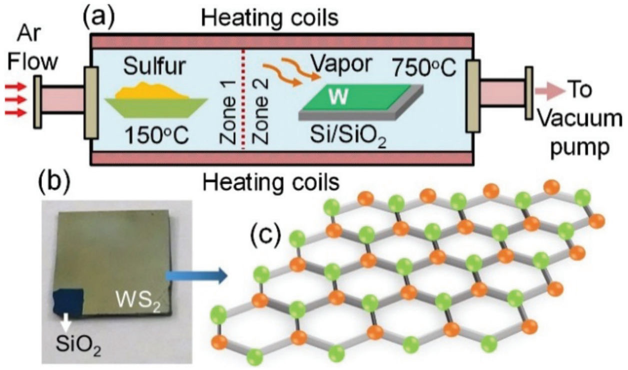

Fig. 1 (a) Schematic of the two-zone CVD growth process for the WS_2 nanosheet using Ar as the carrier gas. (b) A typical CVD synthesized sample showing WS_2 nanosheet on SiO_2. (c) Schematic of hexagonal atomic planar structure of WS_2 showing W and S atoms.

Material characterization

Raman spectroscopy with a laser excitation wavelength of 532 nm (Horiba Scientific) was performed to study the as-grown WS_2 nanosheet, and monolayer/bilayer/multilayer graphene. The WS_2 nanosheet, coated on a glass substrate, was subjected to UV/visible absorption measurement to acquire the values of optical bandgap and transmittance using a Camspec M550 Double-Beam Scanning UV/Vis Spectrophotometer (in the spectral range of 200 nm–900 nm). The surface profile of the WS_2 nanosheet was analysed by Dimension 3100 atomic force microscopy (AFM).

Solar cell fabrication and characterization

Al thin films of 100 nm were deposited on three glass substrates by the electron beam evaporation method. The CVD-grown WS_2 nanosheets were transferred onto each of the Al-coated glass substrates by a manual transfer process. Monolayer, bilayer and multilayer graphene sheets, synthesized by the CVD method, were subsequently transferred onto the three Al-coated substrates. The stacked structures glass/Al/WS_2/graphene were annealed at 100 °C for five minutes to remove any excess solvents present in the samples. In our experiment, monolayer and multilayer graphene sheets were as-grown on Cu and Ni foils, respectively. The bilayer graphene was obtained by stacking two monolayer graphene grown on Cu. Three Schottky barrier solar cells, having different stacked structures of (i) glass/Al/WS_2/monolayer graphene, (ii) glass/Al/WS_2/bilayer graphene, and (iii) glass/Al/WS_2/multilayer graphene, were characterized to explore the material interfacial properties and photovoltaic characteristics. Fig. 2 shows a combined schematic view of the fabricated three Schottky barrier solar cells employing WS_2 nanosheet as a photoactive semiconductor with monolayer, bilayer, and multilayer graphene as the Schottky contacts. The current-density-*vs.*-voltage (*J*–*V*) characteristics of the Schottky barrier solar cells were measured under both dark conditions and standard AM 1.5 illumination using an Agilent B1500A semiconductor device analyzer. A calibrated Xe arc lamp was used to simulate the natural solar light. The Schottky barrier solar cells were illuminated through the graphene contacts as shown in Fig. 2.

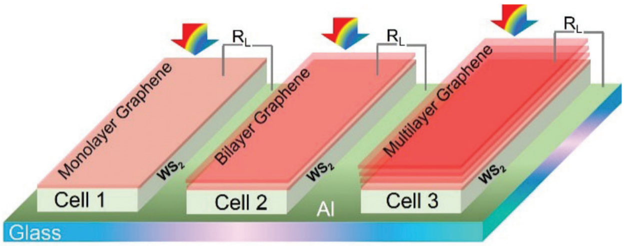

Fig. 2 A combined schematic structure of the three fabricated Schottky barrier solar cells using Al as the ohmic contact for WS_2 nanosheet, while monolayer, bilayer, and multilayer graphene were used as Schottky contacts. The devices are labelled as cell-1, cell-2 and cell-3, respectively.

Results and discussion

AFM characterization was performed on the CVD-synthesized WS_2 nanosheet to examine the surface properties. A 30 × 30 μm^2 surface topography scan on the WS_2 nanosheet grown on Si/SiO_2 is shown in Fig. 3(a). A clear difference is observed between the SiO_2 surface and the CVD WS_2 nanosheet. In the same scanning area, the phase image was generated, showing significant contrast between the two materials, as displayed in Fig. 3(b). The AFM line scan measurement was also conducted on the WS_2 nanosheet sample. The average value was considered on the SiO_2 substrate and on the WS_2 nanosheet, confirming the thickness of the WS_2 nanosheet at about ~37 nm, as shown in Fig. 3(c).

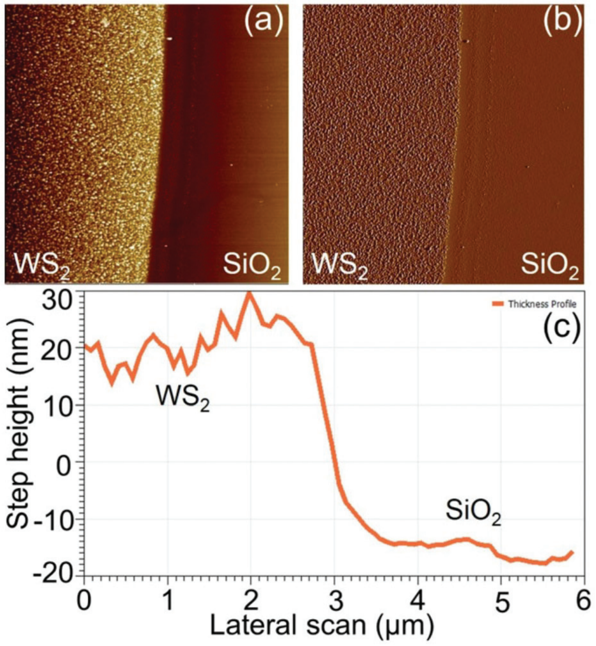

Fig. 3 AFM measurements results of (a) surface morphology of WS_2 nanosheet on SiO_2, (b) phase image indicating the variation of phase between SiO_2 and WS_2 and (c) line-scan corresponding to the surface profile shown in (a) showing the thickness of the WS_2 nanosheet.

Raman spectroscopic measurements were performed to study the monolayer, bilayer and multilayer graphene sheets. The major characteristic peaks of monolayer graphene were observed at 1582 cm^{-1} and 2679 cm^{-1}. The intensity ratio between G and 2D peaks confirms it is monolayer grapheme, as shown in Fig. 4(a). In the case of bilayer graphene, the intensity of G and 2D peaks is observed to be nearly the same, as seen in Fig. 4(b). Multilayer graphene sheets obtained on Ni foil showed dominant G peaks, as illustrated in Fig. 4(c). The intensity ratio between 2D and G peaks of monolayer, bilayer, and multilayer graphene sheets was calculated and shown in Fig. 4(d). It is well known that the 2D peak in graphene originates from double resonance electron-phonon scattering which exhibits significant differences among monolayer, bilayer, and multilayer graphene sheets.

It is expected that the intensity of the G peak increases with the number of graphene layers. As shown in Fig. 4(a)–4(c), the G peak of multilayer graphene is the strongest among all graphene samples. The position and full-width-at-half-maximum of the G-peak are not sensitive to the number of layers. It originates from in-plane vibration of sp^2 carbon with doubly degenerated phonon modes at the center of the Brillouin zone. However, the 2D peak shows significant variation due to the change in the band structure of multilayer graphene. We also observe that all three samples do not show a noticeable D peak in the Raman spectra, confirming a reasonably good quality of graphene. It should be noted that the ratio of 2D and G peaks decreases with the number of graphene layers, as seen in Fig. 4(d). The ratio is much higher for monolayer graphene as compared with bilayer and multilayer graphene sheets, with

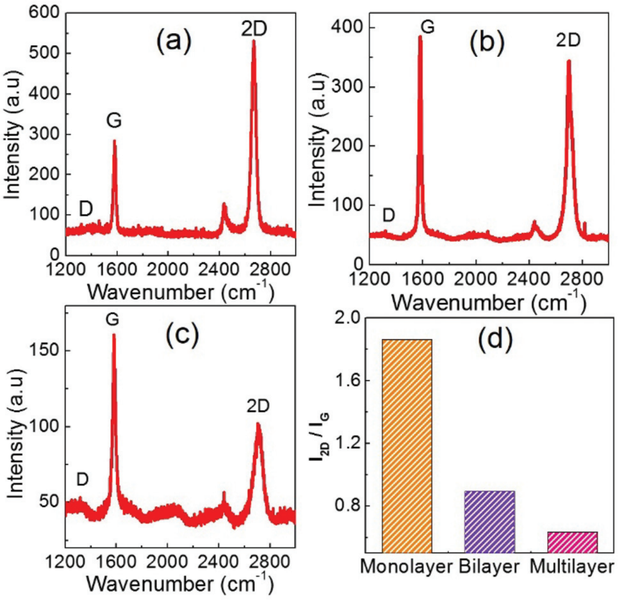

Fig. 4 Raman spectroscopic characterization results of (a) monolayer graphene synthesized on Cu, (b) bilayer graphene obtained by stacking two monolayers, (c) multilayer graphene synthesized on Ni foil, and (d) intensity ratio comparison of the three samples.

multilayer exhibiting the smallest value among all samples, as illustrated in Fig. 4(d).

Two strong active vibrational modes of WS_2 were observed. We confirm the major vibrational Raman modes in the CVD as-synthesized samples from the disappearance of the peak at ~421.3 cm^{-1} (A_{1g} mode). The peak at ~352.8 cm^{-1} with no polarization dependence is the E^1_{2g} mode. Fig. 5(a) shows the Raman spectrum obtained on the WS_2 nanosheet samples in the wavenumber range of 300 cm^{-1}–500 cm^{-1}. The E^1_{2g} peak (352.8 cm^{-1}) represents in-plane atomic vibration in the WS_2 lattice, while the A_{1g} peak (421.3 cm^{-1}) is associated with the out-of-plane vibrational mode. The E^1_{2g} mode involves in-plane displacement of both transition metal and chalcogen atoms, while the A_{1g} mode involves only chalcogen atoms. A schematic of the two Raman active vibrational modes of WS_2 is illustrated in Fig. 5(b). The values obtained for the representative peaks are slightly different, when compared to those of the bulk crystals (355 cm^{-1} and 421 cm^{-1}, respectively). The very slight shift might be from the unintentional impurity contents present on the surface.

The Lorentzian double-peak-fit was performed on the Raman spectra obtained from the three nanosheet samples to extract the values of FWHM, and a typical fitting is shown in Fig. 5(c), performed on sample 2. The two Lorentzian fits yield the peaks corresponding to the experimental data at both signature values. All the three samples showed FWHM values approximately ~18 for E^1_{2g} and 8 for A_{1g}, respectively, suggesting that the CVD-grown WS_2 nanosheets are highly crystalline in nature with negligible structural deformation (that could be introduced during the SiO_2 wet etching step and the subsequent transferring process between different substrates). The post-treatment, *i.e.*, annealing at 1000 °C after growth, helps in forming the highly crystalline nanosheets. Fig. 5(d) shows the calculated difference in the wavenumber of E^1_{2g} and A_{1g} vibrational modes for the three samples. The nearly-equal difference values in wavenumber suggest that the three nanosheet samples possess nearly identical characteristics, synthesized by the same growth process.

Three WS_2 nanosheets were consecutively transferred onto the glass substrate for conducting characterization using UV-visible optical absorption spectroscopy. From the AFM profiling measurement, it is confirmed that each nanosheet is about ~37 nm thick and hence the transfer process yields a 111 nm stack. The WS_2 stack for UV visible absorption measurement was used for subsequent fabrication of a solar cell with graphene as a Schottky contact. Fig. 6 shows the measured optical transmittance of the WS_2 nanosheet in the wavelength range of 200 nm–900 nm. The nanosheet exhibits a maximum optical transmittance of ~43% in the longer wavelength region, while showing very efficient photo-absorption in the visible spectral window. The optical absorbance spectrum corresponding to the transmittance is shown in Fig. 6. A strong photo-absorption in the wavelength range starting from 200 nm to 900 nm suggests that the WS_2 nanosheet is desirable for solar energy harvesting. We also calculated the optical bandgap of the WS_2 nanosheet from the measured optical transmittance using the Tauc plot method *via* the relationship $\alpha h\nu \propto (h\nu - E_G)^{1/2}$, where α is the absorption coefficient of the WS_2 nanosheet, $h\nu$ is the incident photon energy, and E_G is the optical bandgap (that determines the photo-absorption spectral range). The bandgap is calculated to be ~1.3 eV from the transmittance spectrum shown in Fig. 6. A dominant photo-absorption associated with a 1.3 eV bandgap is highly favourable for solar cell design, as this spectral range suits well thin-

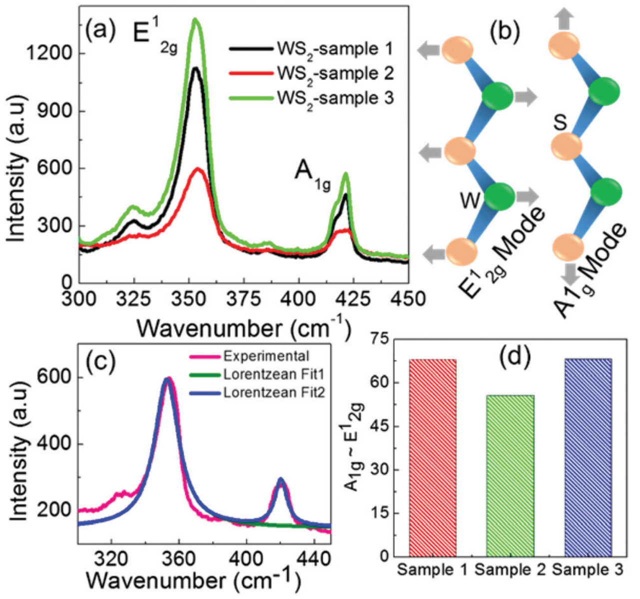

Fig. 5 (a) Raman spectra of three CVD synthesized WS_2 nanosheet samples used for solar cell fabrication showing two major vibrational modes. (b) Schematic of atomistic view of the two modes illustrating the direction of atomic movements. (c) Double peak Lorentzian fit of the Raman spectrum for sample 2. (d) The calculated wavenumber difference of two vibrational modes for three WS_2 nanosheet samples.

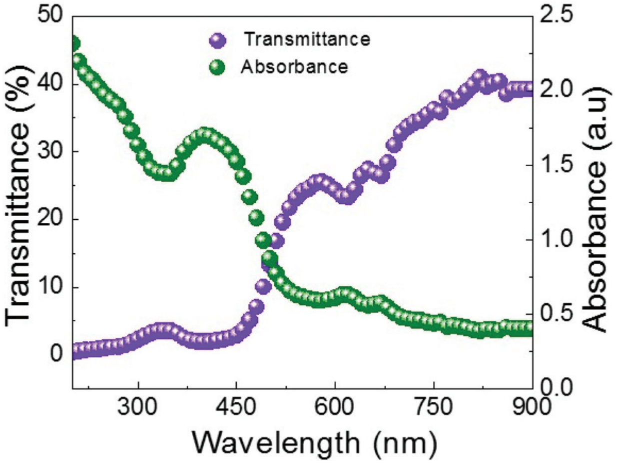

Fig. 6 Measured UV-visible absorbance and transmittance of the WS_2 nanosheet exhibits strong photo-absorption in the spectral window of 200 nm–900 nm and the corresponding transmittance shows a maximum value of ~43% at a longer wavelength region with a calculated optical bandgap value of 1.3 eV.

film semiconductors such as amorphous Si, CdSe, CdTe and CdS.

Three Schottky barrier solar cells (cell-1 with monolayer graphene on WS_2, cell-2 with bilayer graphene on WS_2, and cell-3 with multilayer graphene on WS_2) were characterized under dark conditions and AM1.5 illumination. The graphene induced Schottky barrier in the WS_2 nanosheet is used to develop an electric field at the graphene/WS_2 junction, used for efficient electron–hole pair dissociation in the solar cells. The built-in electric field at the graphene–WS_2 junction points towards the graphene contact from the WS_2. Thus, the electron transport occurs in the opposite direction, from the WS_2 to the Al ohmic contact. The holes generated in the valence band of the WS_2 nanosheet are transported towards the graphene contact along the electric field direction.

Fig. 7(a) shows the J–V characteristics of the three devices under AM1.5 illumination calibrated by a standard solar cell. The output power characteristics as a function of the applied voltage are shown in Fig. 7(b). The Schottky-barrier solar cell employed monolayer graphene as a contact on WS_2 (cell-1) exhibits the key device metrics of J_{SC} (short-circuit current density), V_{OC} (open-circuit voltage), P_{MAX} (maximum power), and η (photo-conversion efficiency) of 9.2 mA cm^{-2}, 640 mV, 1.6×10^{-3} W, and 2.3%, respectively. The cell-2 (bilayer graphene contact on WS_2) shows J_{SC}, V_{OC}, P_{MAX} and η as 14.2 mA cm^{-2}, 680 mV, 2×10^{-3} W, and 2.9% respectively. For cell-3 (multilayer graphene contact) the J_{SC}, V_{OC}, P_{MAX} and η are 16 mA cm^{-2}, 700 mV, 2.3×10^{-3} W, and 3.3% respectively. It should be noted that the changes in solar cell performance metrics are influenced only by the graphene contact (made of varying number of layers), as the WS_2 nanosheet thickness remains the same. While improvement of solar cell performance is expected by increasing the WS_2 nanosheet thickness, the presented effort is focusing only on the effect of graphene contacts.

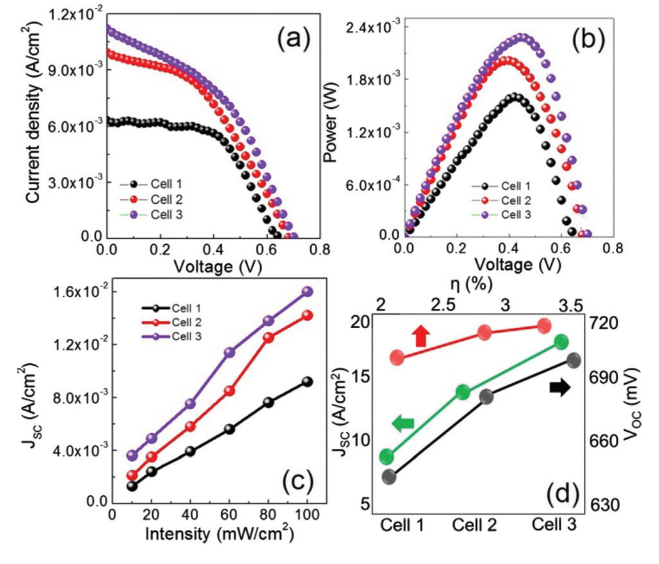

Fig. 7 Schottky barrier solar cell performance: (a) J–V characteristics of three solar cells under AM1.5 illumination, (b) output power, (c) light intensity dependence of J_{SC} values, and (d) comparison of performance metrics showing J_{SC}, V_{OC} and η for different solar cells.

The J_{SC} characteristics of the Schottky barrier solar cells were measured under different illumination conditions, as shown in Fig. 7(c). A nearly linear increase in J_{SC} with incident light intensity is observed for all three devices. The photo-carrier generation is significantly impacted by the incident light intensity, therefore drastically changing the J_{SC} value. A larger increase in J_{SC} is observed in the Schottky barrier solar cell with multilayer graphene contact as compared with other two devices, suggesting that multilayer graphene would be the desirable contact configuration for the Schottky barrier solar cell.

Fig. 7(d) summarizes the measured key metrics of the solar cell (J_{SC}, V_{OC} and η) for the three Schottky barrier solar cells with monolayer, bilayer, and multilayer graphene contacts. Cell-3 shows exceptional value in V_{OC} as compared with cell-1 and cell-2, offering an insight about the major change in the quasi-Fermi level splitting due to optical illumination. The difference in the J_{SC} value among all three solar cells would be due to efficient electron–hole pair separation and collection as a result of significant modification in Schottky barrier behaviour by bilayer and multilayer graphene contacts. Therefore, we attribute the distinction in overall photovoltaic performance in the solar cell to the critical impact of graphene contacts and the associated Schottky junction properties.

Fig. 8 shows the energy-band diagram of the graphene–WS_2 nanosheet Schottky barrier solar cell (as shown in Fig. 2) with reference to the vacuum level (E_0). Photons incident on the device through the graphene layer and excite electrons from the valence band (E_V) to the conduction band (E_C) of the WS_2 nanosheet, leaving holes in the valence band. The electric field (E_J) developed at the graphene–WS_2 interface, pointing towards the graphene contact, drives the photo-generated electrons towards the Al electrode. The parameters ϕ_G, ϕ_{WS_2}, and ϕ_B represent the work function of graphene, WS_2, and the Schottky

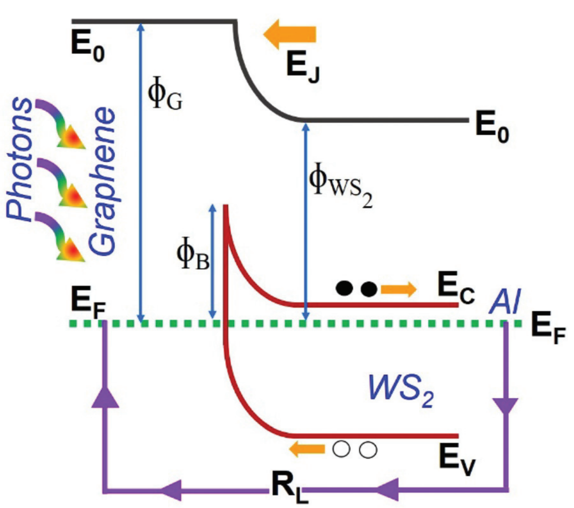

Fig. 8 Schematic of energy level alignment at the graphene–WS_2 interface illustrating Schottky barrier height, junction electric which drives electron–hole transport towards their respective electrodes.

barrier height, respectively. The parameter E_F represents the position of the Fermi level for graphene, the WS_2 nanosheet and Al contact. The transport pathway of photo-generated electrons starting from E_C of the WS_2 nanosheet to E_F of the Al contact and to graphene through an external load (R_L) is illustrated.

In conventional bulk or thin-film semiconductors such as Si and GaAs, the surface is not self-terminated. Since the lattice periodicity is interrupted, the surface possesses a huge density of unsaturated dangling bonds which act as recombination centers limiting solar cell performance. The surface recombination velocity of photo-generated carriers is greatly influenced by the surface traps, resulting in a key recombination process. 2D layered semiconductors, by nature, are individual atomic planes coupled *via* weak van der Waals forces. The surface is a self-terminated atomic plane with no dangling bonds. Therefore, in principle the surface recombination velocity is expected to be extremely low, as compared to conventional bulk and thin-film semiconductors. The low surface recombination velocity helps in facilitating an efficient photo-generated carrier collection at the electrode, yielding solar cells with significantly improved photocurrent.

The *J–V* characteristics under dark conditions represent the interface material quality that directly impacts carrier transport and recombination in solar cells. Electron transport under dark conditions is in the opposite direction to that under illumination. If dark current is minimized, the net photocurrent increases. Fig. 9(a) shows the dark *J–V* characteristics of the three Schottky barrier solar cells in a forward-bias region of 0 V–1 V. The onset voltage of the dark current is lower in cell-3 (multilayer graphene contact), and is shifted by about a hundred meV in the positive bias region for cell-2 and cell-3, as shown in Fig. 9(a). The reduced dark current density, positive shift of the onset voltage, and increased photocurrent indicate that the multilayer graphene contact helps in reducing electron capturing from the conduction band of the WS_2 and hole capturing from the valence band, and eventually controls the trap-assisted recombination process in the WS_2. Fig. 9(a) inset shows the semi-log plot of the dark *J–V* characteristics of the three solar cells, showing distinct behavior in the forward bias region (from 0 V–1 V).

The dark current density is analyzed in the low- (0.2 V–0.4 V) and medium-forward-bias regions (0.5 V–0.8 V) to study the recombination possibilities at the bulk of WS_2 and graphene–WS_2 interface, as well as the impact of graphene on carrier transport and recombination. Fig. 9(b) and (c) show the curve fitting by a single-diode model performed on all the three devices in the low- and medium-forward-bias regions, respectively. The linear region in the semi-log plot of *J–V* characteristics is fit into the single-diode model to extract the dark saturation current density (J_0),

$$J_D(V) = J_0\left(e^{\frac{qV}{nkT}} - 1\right) \tag{1}$$

Here q is electronic charge, V is the applied voltage to solar cell, n is the ideality factor, k is the Boltzmann constant, and T is temperature at which the solar cell operates (300 K).

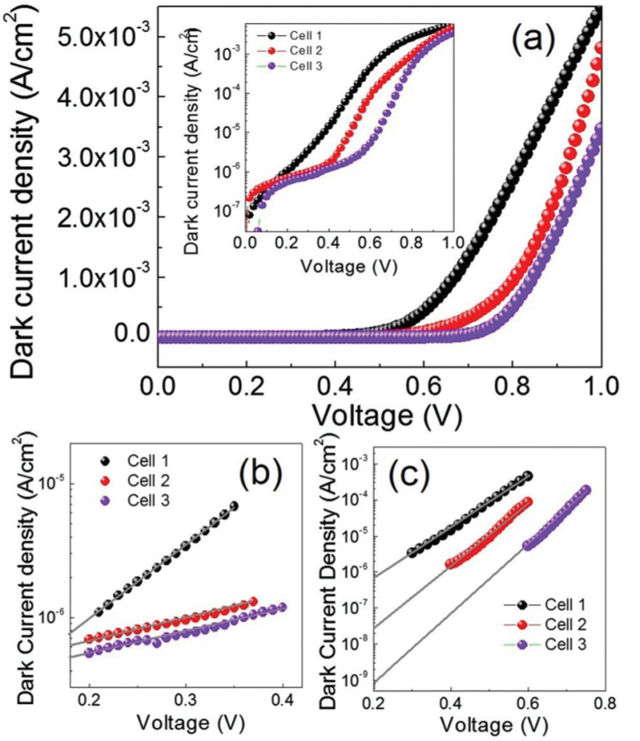

Fig. 9 (a) Dark *J–V* characteristics of the Schottky barrier solar cells with the inset showing the semi-log plot. (b) Fitting with the low-forward-bias diode model to extract the J_0 values for solar cells. (c) Fitting with the medium-forward-bias diode model.

The values of J_0 for three solar cells with different graphene contacts are listed in Table 1. In both conditions, low- and medium-forward-bias regions, cell-3 with multilayer graphene contact exhibits lower J_0 than other two devices. In particular, the diode model fitting at the medium-forward-bias region showed a significantly lower J_0 value for cell-3 than that of cell-1 and cell-2, demonstrating a better control over dark current in device configuration with multilayer graphene contact. This could be the primary cause for the improved photovoltaic performance of the cell-3 as compared with other two devices.

It is known that electron transport occurs in opposite directions under dark and illumination conditions. Lower dark current value confirms the improvement in the illuminated *J–V* characteristics of a solar cell. In other words, the net photocurrent of a solar cell under illumination conditions would be

Table 1 Comparison of saturation current density J_0 values under dark conditions for all the three Schottky barrier solar cells at different forward bias regions, showing the effect of graphene contact

Devices	J_0 (A cm^{-2}) Low forward bias	J_0 (A cm^{-2}) Medium forward bias
Cell-1	7.7×10^{-7}	7.3×10^{-7}
Cell-2	6.2×10^{-7}	2.9×10^{-8}
Cell-3	5.0×10^{-7}	9.3×10^{-10}

adversely affected by an increase in dark current. This can be explained, in a simple way, by eqn (2),

$$J(V) = J_{\mathrm{SC}} - J_{\mathrm{D}}(V) \tag{2}$$

Here, J_{D} is the dark-current density of the solar cell and $J_{\mathrm{D}}(V)$ is the dark-current density as expressed in eqn (1). It is evident that decreasing J_0 would increase the net photocurrent, therefore improving the photovoltaic performance. The Schottky barrier solar cell with multilayer graphene on WS_2 exhibits the lowest dark saturation current density, as listed in Table 1, leading to enhanced photoconversion efficiency. The V_{OC} increases of 20 mV and 60 meV are observed in cell-3 with multilayer graphene contact as compared with cell-2 (bilayer graphene contact) and cell-1 (monolayer graphene contact), respectively, which can be attributed to the better control over dark current using multilayer graphene contact on the WS_2 nanosheet. This can be explained using the following eqn (3):

$$V_{\mathrm{OC}} = \frac{kT}{q}\ln\left(\frac{J_{\mathrm{SC}}}{J_0} + 1\right) \tag{3}$$

It is therefore understood that better capability to suppress dark current can be achieved *via* using highly conductive multilayer graphene, as compared with monolayer and bilayer graphene, which results in improved solar cell performance. The advantage of adopting multilayer graphene as the Schottky contact on the layered semiconductor WS_2 nanosheet is demonstrated through both illuminated and dark *J*–*V* characteristics and the relationship that connects both in eqn (1)–(3).

Conclusions

We demonstrate graphene/2D semiconductor Schottky barrier solar cells with different layer configurations of graphene contacts on the CVD-assembled WS_2 nanosheets. The solar cell performance is significantly improved by incorporating multilayer graphene as the Schottky contact. While the WS_2 nanosheet exhibits the same efficient visible spectral photoabsorption in all three demonstrated solar cells, the multilayer graphene helps in suppressing the dark current much better than monolayer and bilayer graphene, which improves the Schottky barrier solar cell performance. The experimental results point to the possibility of designing all-2D-layered-material-based solar cells with potential advantages in efficient photoelectric conversion, mechanical flexibility, and low material consumption.

References

1 Q. H. Wang, K. K. Zadeh, A. Kis, J. N. Coleman and M. S. Strano, *Nat. Nanotechnol.*, 2012, **7**, 699–712.

2 R. Ganatra and Q. Zhang, *ACS Nano*, 2014, **8**(5), 4074–4099.

3 W. S. Hwang, M. Remskar, R. Yan, V. Protasenko, K. Tahy, S. D. Chae, P. Zhao, A. Konar, H. Xing, A. Seabaugh and D. Jena, *Appl. Phys. Lett.*, 2012, **101**, 013107.

4 Y. Lin, Y. Zeng and A. Javey, *ACS Nano*, 2014, **8**(5), 4948–4953.

5 S. Das, H.-Y. Chen, A. V. Penumatcha and J. Appenzeller, *Nano Lett.*, 2013, **13**(1), 100–105.

6 J. Kang, W. Liu and K. Banerjee, *Appl. Phys. Lett.*, 2014, **104**, 093106.

7 M. Shanmugam, C. A. Durcan and B. Yu, *Nanoscale*, 2012, **4**, 7399–7405.

8 M. Bernardi, M. Palummo and J. C. Grossman, *Nano Lett.*, 2013, **13**(8), 3664–3670.

9 P. Qin, G. Fang, W. Ke, F. Cheng, Q. Zheng, J. Wan, H. Lei and X. Zhao, *J. Mater. Chem. A*, 2014, **2**, 2742–2756.

10 S. Alkis, T. Özta, L. E. Aygün, F. Bozkurt, A. K. Okyay and B. Ortaç, *Opt. Express*, 2012, **20**, 21815–21820.

11 O. L. Sanchez, D. Lembke, M. Kayci, A. Radenovic and A. Kis, *Nat. Nanotechnol.*, 2013, **8**, 497–501.

12 R. B. Jacobs-Gedrim, *et al.*, *ACS Nano*, 2014, **8**(1), 514–521.

13 H. Wang, H. Feng and J. Li, *Small*, 2014, **10**, 2165–2181.

14 T. Stephenson, Z. Li, B. Olsen and D. Mitlin, *Energy Environ. Sci.*, 2014, **7**, 209–231.

15 K. Chang, W. Chen, L. Ma, H. Li, H. Li, F. Huang, Z. Xu, Q. Zhang and J.-Y. Lee, *J. Mater. Chem.*, 2011, **21**, 6251–6257.

16 H. Hwang, H. Kim and J. Cho, *Nano Lett.*, 2011, **11**(11), 4826–4830.

17 L. E. Chaar, L. A. lamont and N. E. Zein, *Renewable Sustainable Energy Rev.*, 2011, **15**, 2165–2175.

18 M. Konagai, *Jpn. J. Appl. Phys.*, 2011, **50**, 030001.

19 S. G. Kumara and K. S. R. K. Rao, *Energy Environ. Sci.*, 2014, **7**, 45–102.

20 Y. F. Makableh, R. Vasan, J. C. Sarker, A. I. Nusir, S. Seal and M. O. Manasreh, *Sol. Energy Mater. Sol. Cells*, 2014, **123**, 178–182.

21 T. Georgiou, *et al.*, *Nat. Nanotechnol.*, 2013, **8**, 100–103.

22 K. F. Mak, C. Lee, J. Hone, J. Shan and T. F. Heinz, *Phys. Rev. Lett.*, 2010, **105**, 136805.

23 M. S. Fuhrer and J. Hone, *Nat. Nanotechnol.*, 2013, **8**, 146–147.

24 W. S. Hwang, *et al.*, *Appl. Phys. Lett.*, 2012, **101**, 013107.

25 R. Gatensby, *et al.*, *Appl. Surf. Sci.*, 2014, **297**, 139–146.

26 L.-Y. Gan, Q. Zhang, Y. Cheng and U. Schwingenschlögl, *J. Phys. Chem. Lett.*, 2014, **5**(8), 1445–1449.

27 S. Yang, S. Tongay, Y. Li, Q. Yue, J.-B. Xia, S.-S. Li, J. Li and S.-H. Wei, *Nanoscale*, 2014, **6**, 7226–7231.

28 S. Yang, Y. Li, X. Wang, N. Huo, J.-B. Xia, S.-S. Lia and J. Li, *Nanoscale*, 2014, **6**, 2582–2587.

29 S. Z. Butler, *et al.*, *ACS Nano*, 2013, **7**(4), 2898–2926.

30 G. Eda, H. Yamaguchi, D. Voiry, T. Fujita, M. Chen and M. Chhowalla, *Nano Lett.*, 2011, **11**(12), 5111–5116.

31 R. A. Gordon, D. Yang, E. D. Crozier, D. T. Jiang and R. F. Frindt, *Phys. Rev. B: Condens. Matter*, 2002, **65**, 125407.

32 Y.-H. Lee, *et al.*, *Adv. Mater.*, 2012, **24**, 2320–2325.

33 Y. Zhang, *et al.*, *ACS Nano*, 2013, **7**(10), 8963–8971.

34 Y. C. Lin, *et al.*, *Nanoscale*, 2012, **4**, 6637–6641.

35 A. K. Geim and K. S. Novoselov, *Nat. Mater.*, 2007, **6**, 183–191.

36 C. M. Weber, *et al.*, *Small*, 2010, **6**, 184–189.

37 C. X. Guo, *et al.*, *Angew. Chem., Int. Ed.*, 2010, **49**, 3014–3017.

38 W. Zhu, V. Perebeinos, M. Freitag and P. Avouris, *Phys. Rev. B: Condens. Matter*, 2009, **80**, 235402.

39 S. Bertolazzi, D. Krasnozhon and A. Kis, *ACS Nano*, 2013, **7** (4), 3246–3252.

40 K. Roy, *et al.*, *Nat. Nanotechnol.*, 2013, **8**, 826–830.

41 J. Yoon, *et al.*, *Small*, 2013, **9**, 3295–3300.

42 L. Britnell1, *et al.*, *Science*, 2012, **335**, 947–950.

43 M. Bernardi, M. Palummo and J. C. Grossman, *Nano Lett.*, 2013, **13**(8), 3664–3670.